*Article*

# Repurposing Face Masks after Use: From Wastes to Anode Materials for Na-Ion Batteries

Silvia Porporato [1,2], Mattia Bartoli [3], Alessandro Piovano [1,2], Nicolò Pianta [4], Alberto Tagliaferro [5], Giuseppe Antonio Elia [1,2], Riccardo Ruffo [2,4] and Claudio Gerbaldi [1,2,*]

1. GAME Lab, Department of Applied Science and Technology, Politecnico di Torino, Corso Duca Degli Abruzzi, 24, 10129 Torino, Italy
2. National Reference Center for Electrochemical Energy Storage (GISEL)—INSTM, Via G. Giusti 9, 50121 Firenze, Italy
3. Center for Sustainable Future Technologies (CSFT), Istituto Italiano di Tecnologia (IIT), Via Livorno 60, 10144 Torino, Italy
4. Department of Materials Science, University of Milano Bicocca, Via Cozzi 55, 20125 Milano, Italy
5. Carbon Group, Department of Applied Science and Technology, Politecnico di Torino, Corso Duca Degli Abruzzi, 24, 10129 Torino, Italy
* Correspondence: claudio.gerbaldi@polito.it

**Abstract:** Nowadays, face masks play an essential role in limiting coronavirus diffusion. However, their disposable nature represents a relevant environmental issue. In this work, we propose the utilization of two types of disposed (waste) face masks to prepare hard carbons (biochar) by pyrolytic conversion in mild conditions. Moreover, we evaluated the application of the produced hard carbons as anode materials in Na-ion batteries. Pristine face masks were firstly analyzed through infrared spectroscopy and thermogravimetric analysis. The pyrolysis of both mask types resulted in highly disordered carbons, as revealed by field-emission scanning electron microscopy and Raman spectroscopy, with a very low specific surface area. Anodes prepared with these carbons were tested in laboratory-scale Na-metal cells through electrochemical impedance spectroscopy, cyclic voltammetry and galvanostatic cycling, displaying an acceptable specific capacity along a wide range of current regimes, with a good coulombic efficiency (>98% over at least 750 cycles). As a proof of concept, the anodes were also used to assemble a Na-ion cell in combination with a $Na_3V_2(PO_4)_2F_3$ (NVPF) cathode and tested towards galvanostatic cycling, with an initial capacity of almost 120 $mAhg^{-1}$ (decreasing at about 47 $mAhg^{-1}$ after 50 cycles). Even though further optimization is required for a real application, the achieved electrochemical performances represent a preliminary confirmation of the possibility of repurposing disposable face masks into higher-value materials for Na-ion batteries.

## 1. Introduction

In 2019, the outbreak of coronavirus disease 2019 (COVID-19) hit the whole world [1]. Disposable face masks (FMs) became fundamental in limiting the infection spread and turned into a daily item for the population. Their consumption has boosted up tremendously, and their environmental burden is now a matter of ongoing debate, becoming a real issue due to the absence of a defined FM recycling protocol, with the subsequent generation of a large amount of plastic and microplastic residues [2,3]. The lack of an adequate procedure is ascribable to two main facts: first, FMs present a high risk of contamination from several diseases, even those different from COVID-19 [4]; in addition, FMs possess a heterogeneous composition, where both polymers and metallic compounds coexist, making difficult to establish a reliable recycling/repurposing platform [5].

The COVID-19 outbreak happened so rapidly that it caused the overall FM value chain to be unready for the volume of waste streams to process [6,7]. The conversion of

production lines to sustainable materials has still not matched the need to face the ongoing pandemic [8]. Accordingly, virtuous disposal routes for managing FM waste stream should be enforced. Thermochemical routes have been very promising, representing at the same time both disinfection routes [9] and a multicomponent conversion platform [10]. Park et al. [11] described the valorization of FMs through pyrolytic conversion for the production of drop-in fuels, while Lee et al. [12] used catalytic pyrolysis for FM conversion to aromatic hydrocarbon mixtures. Nevertheless, these studies neglected the solid residue formed during the thermal degradation of FMs. Indeed, FM-derived char shows interesting properties, even allowing its use in the electrochemical storage field as an electrode material, as already demonstrated for supercapacitors [13] and lithium–sulfur batteries [14]. These applications are of great interest due to the increased accountability of central governments in the battle against climate change and in developing alternatives to oil-derived fuels as energy reservoirs for mobility and industry. Nonetheless, the energy transition requires the implementation of technologies based on abundant and low-cost elements to mitigate the current scarcity of many key Li-ion battery (LIB) materials, such as lithium and transition metals (e.g., Co and Ni) [15].

In this context, sodium-ion batteries (NIBs) represent a solid alternative to traditional LIBs thanks to the elemental abundance of the key materials (e.g., Na, Mn, Fe), their expected low costs per kWh and their relatively benign environmental nature [16,17].

Additionally, NIBs have the great advantage of being essentially a "drop-in" technology [18,19]. NIBs can maintain the core of the roll-to-roll system optimized for LIB manufacturing, sharing the same architecture, similar working mechanisms and components. At the material level, many efforts have been dedicated to developing sodium-based cathodes characterized by high capacity and high-power capability [20] and identifying a suitable negative electrode. Graphite is the predominant intercalation material in LIBs, thanks to the high theoretical capacity and the presence of a flat potential plateau at a low potential [21]. However, graphite cannot be used as an intercalation compound in NIBs due to the inability of graphite to accommodate $Na^+$ ions [22–24], requiring the design of other suitable host materials. Several carbon materials have been studied, evidencing that good performances are generally achieved by amorphous variants, owing to their different microstructure and sodium storage mechanism [25].

Starting from these premises, hard carbon (HC) has been identified as an excellent candidate for NIBs. HC exhibits a high sodium capacity, low redox potential, good structure stability and relatively low cost [26]. Moreover, it can be obtained from several different precursors, such as biomass materials and polymers [27]. The careful choice of the precursor is essential, as it influences the morphologies of HC and thus the electrochemical performances of the resulting NIB anodes. For instance, different polymeric sources show similar chemical composition and structural ordering, but a varied microporosity. On the other hand, the same materials present essential differences regarding reversible and irreversible capacities, and no correlation with the porous structural characteristics has been found yet [28].

The synthesis of HC by direct pyrolysis of precursors is relatively simple and manageable to scale up, but its practical application in commercial batteries is still limited. Indeed, HC exhibits low reversible capacities, and thus low first-cycle coulombic efficiencies due to sodium consumption when forming the solid electrolyte interface (SEI) layer [29]. Moreover, the SEI itself is prone to evolve during cycling, which is detrimental to the long-term cycling of the batteries [30]. Lastly, the ion storage mechanism still presents many questions. In order to overcome these issues, further mechanistic studies, material design and electrolyte optimization are necessary.

In the framework of the national project PRIN-TRUST, funded by the Italian Government, Ministry of Education, Universities and Research, our research was focused on developing novel optimized electrode/electrolyte materials to achieve sustainable, high-performing, all-solid-state sodium-ion batteries able to meet the present challenges of large-scale energy storage and integration of intermittent renewable sources. In this

context, we reported the pyrolytic conversion of two types of FMs, both surgical and FFP (Filtering Face Piece)-2 (common acronym according to the European standard), into HCs, which were then tested as anode materials for NIBs. The pyrolysis was carried out in very mild conditions (800 °C) and without any previous treatment, in contrast to a recent work of Lee et al. [31] in which FMs were at first soaked in sulfuric acid at 98% at 120 °C for several hours and then carbonized at about 2000 °C. The procedure proposed in this work is intended to be a simple and cheap strategy to conveniently repurpose a problematically abundant waste, as face masks have indeed become globally. FMs were firstly characterized from a structural point of view by means of IR spectroscopy and thermogravimetric analysis (TGA). The pyrolyzed product was characterized through Raman spectroscopy and field-emission scanning electron microscopy (FESEM) and then used to produce anodes, the electrochemical performances of which were evaluated by means of cyclic voltammetry (CV) and galvanostatic cycling (GC) also coupled with electrochemical impedance spectroscopy (EIS). Lastly, the practical applicability as NIB anode material of the so prepared HCs from FMs was confirmed by assembling a full cell with high working potential $Na_3V_2(PO_4)_2F_3$ (NVPF) as the cathode [32].

## 2. Materials and Methods

### 2.1. Materials and Preparation

Wasted surgical and FFP2 face masks were collected, and their metal parts were removed. The two types of masks were pyrolyzed separately, and the resulting powders were used without any further purification, additives or activation protocols. The resulting electrode tapes for electrochemical testing were obtained from a slurry containing 70 wt% of pyrolyzed FM powder as the active material, 20 wt% of C-65 (Imerys, formerly Timcal, Bodio, Switzerland) as the carbon additive and 10 wt% polyvinylidene fluoride (PVdF, Solef 5130 from Solvay, Brussels, Belgium) as the binder. The slurry was obtained by mixing the three components in *N*-methyl pyrrolidone (NMP, supplied by Sigma-Aldrich, St. Louis, MO, USA) and stirring at room temperature (i.e., ≈21 °C) for about 3 h, until homogeneous dispersions were obtained. The resulting dense slurry was cast onto an Al current collector using a doctor-blade. NMP solvent was removed by evaporation at ambient temperature and further drying at 120 °C in vacuum for 24 h prior to utilization. Electrode tapes were subsequently cut into disks of 2.5 cm$^2$ in area, dried at 120 °C under vacuum for 24 h and stored in an Ar-filled dry glovebox (MBraun LABmasterpro ECO glove box, $O_2$ and $H_2O$ < 1 ppm) prior to their assembly and testing in laboratory-scale test cells.

### 2.2. Methods

Wasted surgical and FFP2 face masks were pyrolyzed in a tubular furnace (Carbolite TZF 12/65/550) under a nitrogen atmosphere, with a heating rate of 50 °C/min up to 800 °C. The system was kept at 800 °C for 30 min and cooled down in a nitrogen atmosphere at room temperature. The two resulting carbonaceous materials (biochar) will be referred to from here on as C-surgical and C-FFP2, respectively.

Pristine waste surgical and FFP2 face masks were analyzed through Fourier transform infrared (FT-IR) spectroscopy (Tensor II, Bruker) in attenuated total reflectance (ATR) mode (Platinum ATR diamond, Bruker, Billerica, MA, USA) in the range 600–3500 cm$^{-1}$. They were further investigated through thermogravimetric analysis (TGA) using NETZSCH TG 209F1 Libra in $N_2$ flux with a temperature ramp of 10 °C/min from 30 °C to 900 °C.

Biochar produced from both waste surgical and FFP2 face masks were characterized using a field-emission scanning electron microscope (FESEM, Zeiss Supra-25, Jena, Germany). Raman spectra were collected in the range from 250 to 3500 cm$^{-1}$ using a Renishaw inVia (H43662 model) equipped with a green laser line (514 nm) and a 50× objective. Decomposition of the Raman spectra was focused on the range 1000–2000 cm$^{-1}$ and performed using a Matlab® (vR2020a) homemade software [33]. The average length of the graphitic cluster diameter ($L_a$) was calculated according to the procedure established by Tuinstra and Koenig [34]. The specific surface area of the samples was measured by means of $N_2$

adsorption at −196 °C on a micrometrics Tristar II instrument (Micromeritics Instrument Corporation, Norcross, GA, USA). The Brunauer–Emmett–Teller (BET) model was applied to analyze the data.

### 2.3. Na-Metal and Na-Ion Cell Assembly and Electrochemical Testing

In this work, both lab-scale Na-metal cells and Na-ion cells were assembled and tested. Na-metal cells were assembled using a Whatman GF/A glass wool disk soaked with 200 μL of electrolyte ($NaClO_4$ 1 M in propylene carbonate, Solvionic, Toulouse, France) as the separator. After assembly, the cells were left 4 h at OCV, waiting for equilibration before testing. They were cycled between 0.05 V and 3 V vs. $Na^+$/Na. The pyrolyzed FM powder was used as the active material (mass loading of ca. 1.5 mg/cm$^2$ for both C-surgical and C-FFP2) and Na metal was used as both the counter and reference electrodes.

Na-ion cells assembled using a Whatman GF/A glass wool disk as the separator, soaked with 200 μL of electrolyte ($NaClO_4$ 1 M in propylene carbonate, Solvionic). $Na_3V_2(PO_4)_2F_3$ (NVPF), prepared from $NH_4H_2PO_4$, $V_2O_5$ and NaF precursors heated under an Ar atmosphere at 650 °C [35], was used as cathode (mass loading of 2.0 mg/cm$^2$). The Na-ion cell was galvanostatically cycled at 0.1 mA/cm$^2$ in the 1–4.1 V potential range vs. $Na^+$/Na.

Both cells were galvanostatically cycled at ambient laboratory temperature using an ARBIN BT2000 battery tester. The cells were cycled at different current rates, where the rate denoted as C/n corresponds to a full discharge (or a full charge) in n hours, based on an envisaged theoretical capacity (C) of 350 mAhg$^{-1}$ for the Na/HC cells and 100 mAhg$^{-1}$ for the HC/NVPF full cells.

Electrochemical impedance spectroscopy (EIS) and cyclic voltammetry (CV) were performed using a VMP3 electrochemical workstation from BioLogic Science Instruments (Seyssinet-Pariset, France). EIS measurements were performed at the open circuit potential (OCV) with an oscillating potential of 10 mV in the 300 kHz–0.1 Hz frequency range. CV was performed in the range of 0.05 and 3 V vs. $Na^+$/Na with a scan rate of 0.1 mV s$^{-1}$. Electrochemical tests were performed using ECC-Std test cells (EL-Cell GmbH, Hamburg, Germany). The test cells were assembled inside the Ar-filled glove box to avoid moisture contamination and left for 4 h at OCV before running the measurements.

## 3. Results

### 3.1. Materials Characterization

The FMs were preliminarily characterized by means of IR spectroscopy in the ATR mode. The resulting spectra are shown in Figure 1.
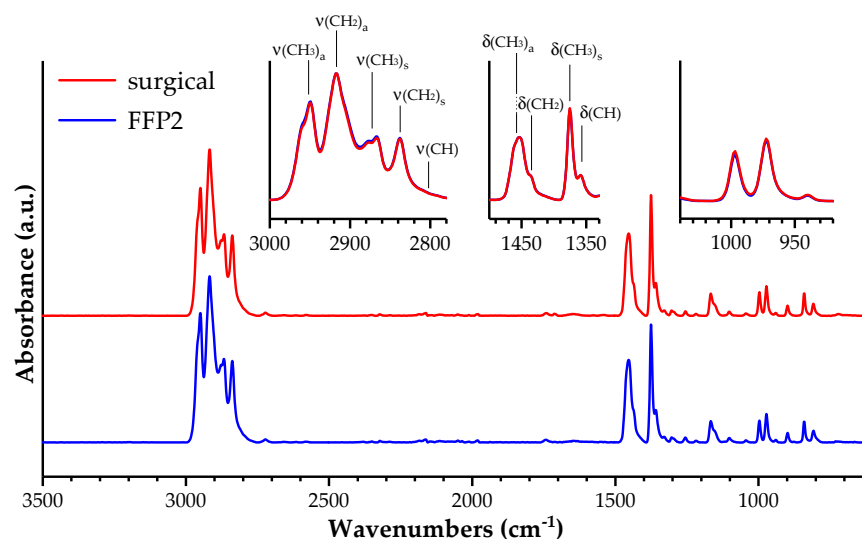


**Figure 1.** FT-IR (ATR mode) of surgical and FFP2 FMs in the range from 500 to 3500 cm$^{-1}$.

Accordingly to Fadare et al. [2], both surgical and FFP2 face masks are mainly composed of fibers of polypropylene (PP). Indeed, both spectra showed the characteristic features of PP, such as the asymmetric and symmetric $\nu(CH_3)$ at 2950 and 2868 cm$^{-1}$ (with shoulders at 2959 and 2877 cm$^{-1}$ because of different phase resonance among neighboring units), the asymmetric and symmetric $\nu(CH_2)$ at 2918 cm$^{-1}$ and 2838 cm$^{-1}$, the asymmetric and symmetric $\delta(CH_3)$ at 1456 cm$^{-1}$ and 1375 cm$^{-1}$, $\delta(CH_2)$ at 1437 cm$^{-1}$ and $\delta(CH)$ at 1359 cm$^{-1}$ [36]. Moreover, the relative intensities of the vibrational modes of the polymer backbone (below 1000 cm$^{-1}$) could be used to acquire information on the propylene stereo-regularity on the basis of the characterization method developed by Burfield and Loi [37]. The method indicated that both samples were characterized by a high degree of isotacticity (up to almost 80%) with no significant differences.

As a matter of fact, the similar composition of the surgical and FFP2 FMs was also reflected in their thermal behavior towards degradation in an inert atmosphere. The two TGA profiles shown in Figure 2 were quite close, with a very sharp weight loss above 450 °C and a minimal solid residue remaining up to 800 °C, this being higher for the surgical FMs than for FFP2 (1.05 against 0.46 wt.%).
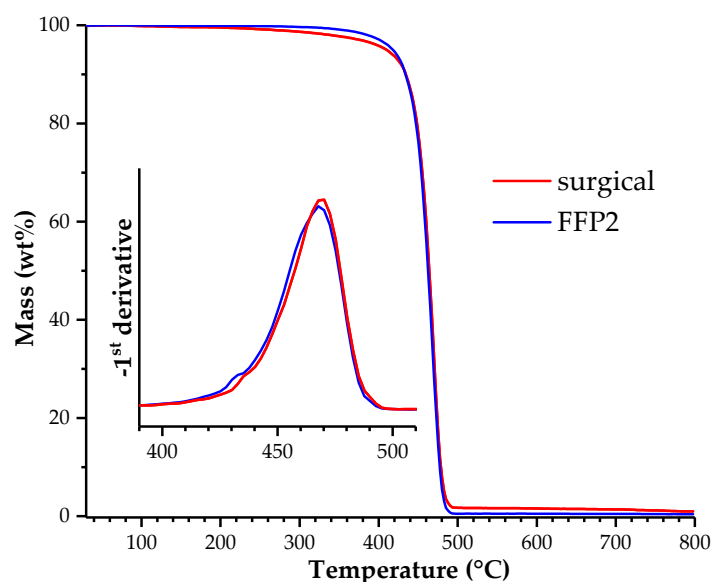


**Figure 2.** TGA curve of surgical and FFP2 facemasks in the range from 30 to 800 °C. The onset was focused on the 400–500 °C range.
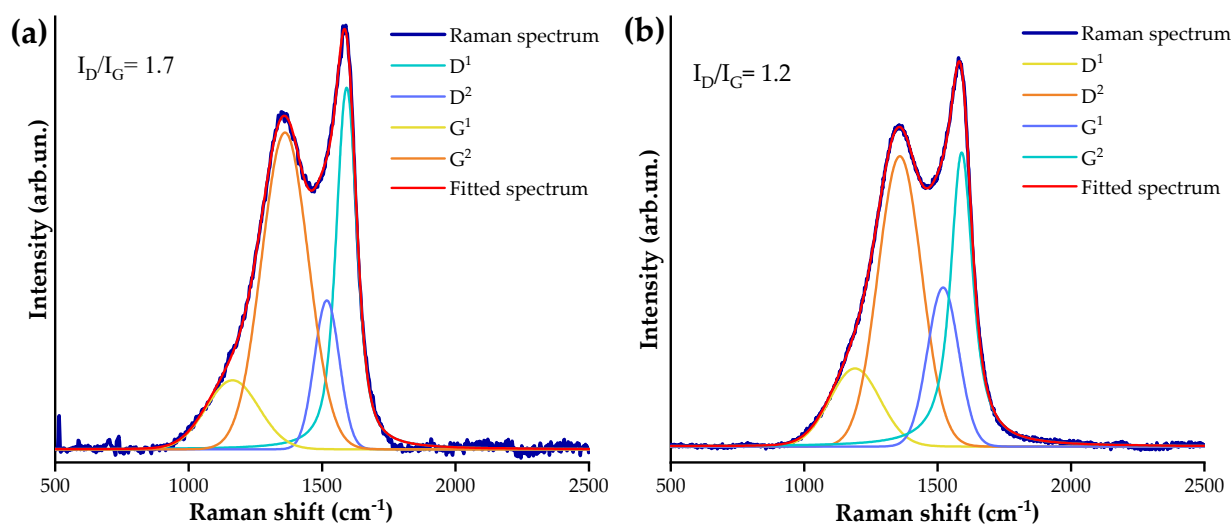
Looking more closely at the TGA profiles, in the surgical sample there was a minor component accounting for less than 3 wt% starting to degrade at a lower temperature (between 300 and 400 °C). This could be associated with the release of heavier hydrocarbons [38]. The inset of Figure 2 shows the first derivative curve indicating that the onset temperature and the maximum degradation rate temperature were slightly higher in the surgical FM sample (Table 1). The difference could be associated with the different topology of the fiber network [39], which is more tightly packed in the case of FFP2 masks (thus promoting a more efficient radical propagation). Furthermore, especially for the FFP2 sample, two components could be distinguished in the first derivative of the degradation profile, likely associated with the two different textile layers typically present in FMs: the melt blown fabric (with an intertwining of small microfibers as the filter) and the spun bond fabric (with thicker fibers for mechanical resistance) [40].

**Table 1.** Main features calculated from TGA curves of surgical and FFP2 FMs.

| Feedstock | $T_{onset}$ (°C) | $T_{max}$ (°C) | Residue (wt.%) [a] |
|---|---|---|---|
| Surgical mask | 430 | 469 | 1.05 |
| FFP2 mask | 426 | 468 | 0.46 |

[a] Calculated as residual wt% at 800 °C.

The pyrolytic conversion of PP-based facemasks led to the production of a small amount of carbon materials and a large hydrocarbon liquid fraction together with a gaseous mixture composed of hydrogen and small chain hydrocarbons that could be directly used as combustible sources [41]. The properties of the solid residue formed were strictly related to several factors ranging from the molecular weight, tacticity and morphology of the starting PP. As shown in the Raman spectra (Figure 3), the pyrolytic char produced from surgical FMs showed an $I_D/I_G$ value up to 1.7, while this value for the C-FFP2 sample was 1.2, with two components for both D and G peaks in both cases, named $D^1/D^2$ and $G^1/G^2$, according to the fitting protocol proposed by Shimodaira and Masui [42]. According to Orlando et al. [43], the Raman spectra of FMs were in good agreement with the presence of highly disordered carbon produced at a temperature of 800 °C [44–46]. The average crystallite size ($L_a$) increased moving from C-surgical to C-FFP2, reaching 26 Å and 37 Å, respectively, supporting the greater organization degree of C-FFP2.



**Figure 3.** Raman spectra of C-surgical (**a**) and C-FFP2 (**b**) in the range between 500 and 2500 cm$^{-1}$.

The morphology of the pyrolytic char produced from the surgical FMs (Figure 4a,b) was characterized by particles having sizes in the range of a hundred microns with few submicrometric carbon particles attached, similar to what was observed by Yousef et al. on other FM-derived carbon materials [47]. The particle size distribution of the FFP2 FMs was slightly different, with an average size lower than 1 μm. The different morphology was in good agreement with the specific surface area, which was 2.1 m$^2$ g$^{-1}$ in the case of C-surgical and 10.2 m$^2$ g$^{-1}$ in the case of C-FFP2, as measured by N$_2$ physisorption analysis at −196 °C.
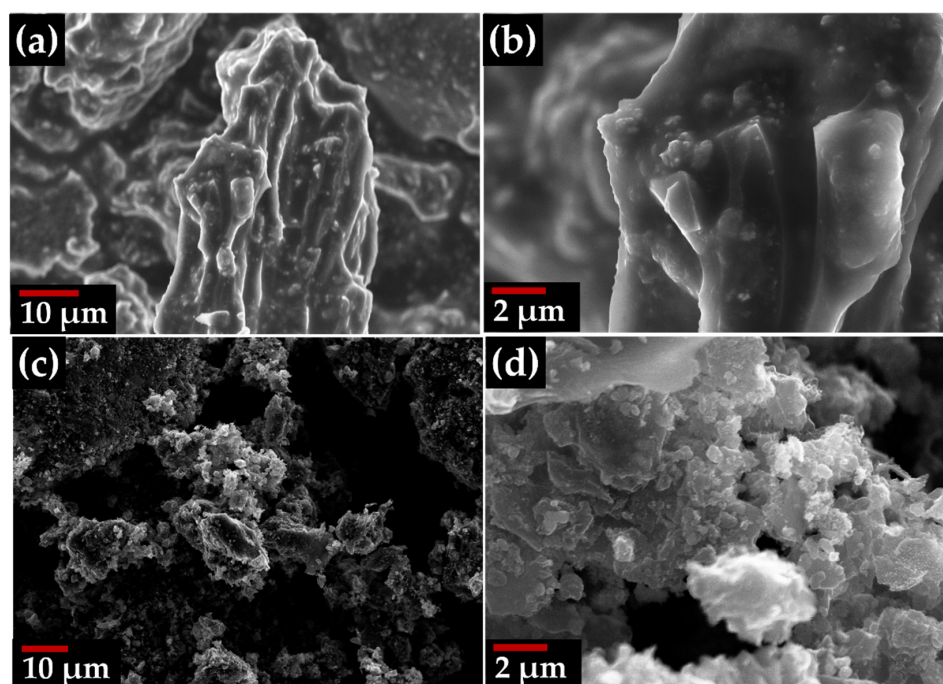
**Figure 4.** FESEM images of C-surgical (**a**,**b**) at different magnification) and C-FFP2 (**c**,**d**) at different magnification).

### 3.2. Electrochemical Behaviour in Lab-Scale Cells

C-surgical and C-FFP2 were tested in Na-metal lab-scale test cells by cyclic voltammetry (Figure 5) in the voltage range between 0.05 and 3 V vs. $Na^+/Na$. During the first cycle, the solid electrolyte interphase (SEI) formation occurred in the range 0.6–0.2 V. The SEI formation is an irreversible and essential process since it prevents further parasitic reactions, enabling the correct cell cycling [48]. The ratio between the integrated areas of the oxidation and reduction profiles permitted the evaluation of the system reversibility: for C-surgical (Figure 5a), the process was 45% reversible in the first cycle, increasing to 86% in the fourth one, while C-FFP2 (Figure 5b) showed an initial 37% reversibility, increasing to 86% at cycle 4. As previously mentioned, the low initial reversibility was imputable to the SEI formation, while in the following cycles, the SEI reached stabilization and acted as a protective layer. In the following cycles, the broad peak in the 0.05–1 V range was associated with the reversible redox process of Na intercalation/absorption in the biochar composite electrode.

The electrochemical impedance spectroscopy (EIS) was measured at open circuit voltage (OCV) after 3 h of rest at OCV and after the cyclic voltammetric test (the corresponding Nyquist plots are shown in Figure 6). Both the fresh cells were characterized by a very low intercept with the real axis (around 5 $\Omega$), corresponding to a very low bulk resistance ($R_b$, mainly associated with the resistance of the electrolyte). The semicircle amplitude was associated with the charge transfer resistance ($R_{ct}$) of $Na^+$ ion diffusion between the electrode and the electrolyte. In contrast, the final straight line in the low-frequency range was associated with a Warburg capacitance, associated with the diffusion of ions [49,50]. After 3 h, $R_{ct}$ increased for both samples (up to 100 $\Omega$ in the real part for C-surgical), thus it was most likely associated with the interfacial layer growth between the electrode and the electrolyte (SEI) [51]. Finally, after voltammetric cycling (blue square spectra), the overall cell resistance decreased, most likely suggesting a stabilization of the SEI upon cycling, indicating a much easier diffusion of $Na^+$ ions from the electrolyte to the electrode after a few electrically promoted cycles [50].
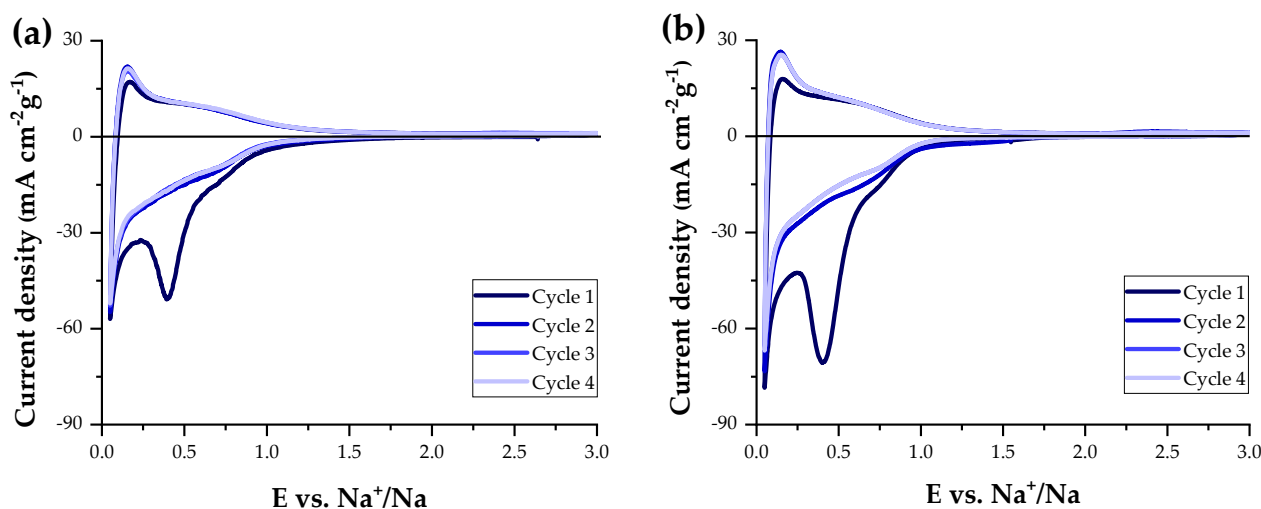
**Figure 5.** Cyclic voltammetric profiles of C-surgical (**a**) and of C-FFP2 (**b**) in 1 M NaClO$_4$ in PC recorded at a scan rate of 0.1 mV s$^{-1}$ in the 0.05–3 V vs. Na$^+$/Na range.
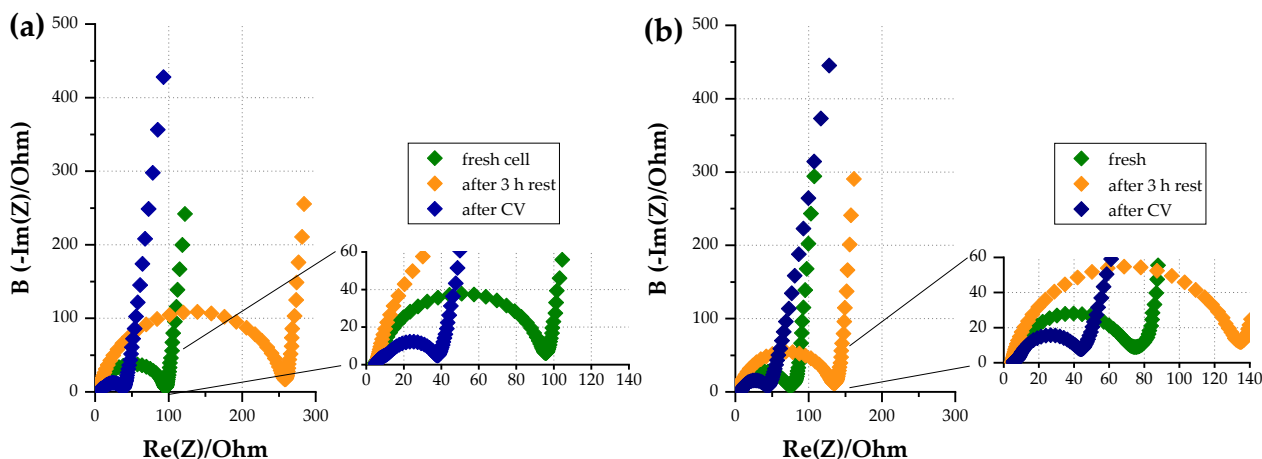


**Figure 6.** EIS spectra of C-surgical (**a**) and of C-FFP2 (**b**) in 1 M NaClO$_4$ in PC vs. Na, recorded at three different stages, i.e., just after assembling the cell, after 3 h of rest at OCV and after the cyclic voltammetric analysis shown in Figure 5.

C-surgical and C-FFP2 showed similar behavior during galvanostatic cycling, as seen in Figure 7. Plots (a) and (d) highlight the charge/discharge profiles of C-surgical and C-FFP2, respectively, in a Na-metal cell with the configuration Na/NaClO$_4$/C at different current regimes (C/20, C/10, C/5, C/2 and 1C) in the 0.05–3 V vs. Na$^+$/Na range. Typical sloping profiles for hard carbon anodes upon reversible insertion/deinsertion of Na$^+$ ions were observed. The specific capacity delivered by the cell exceeded 100 mAh g$^{-1}$ for C-surgical and 115 mAhg$^{-1}$ for C-FFP2 during the initial cycles at a C/20 rate. A capacity drop occurred upon doubling the current rate to C/10, delivering 82 and 98 mAh g$^{-1}$, respectively. Further increases in the current rate caused a progressive decrease in the specific capacity values, which were 64 and 80 mAh g$^{-1}$ at C/5, 43 and 58 mAh g$^{-1}$ at C/2, and 30 and 45 mAh g$^{-1}$ at 1C. Overall, the overpotential increase while increasing the C-rate was rather limited, accounting for the good electronic conductivity of the composite electrodes.
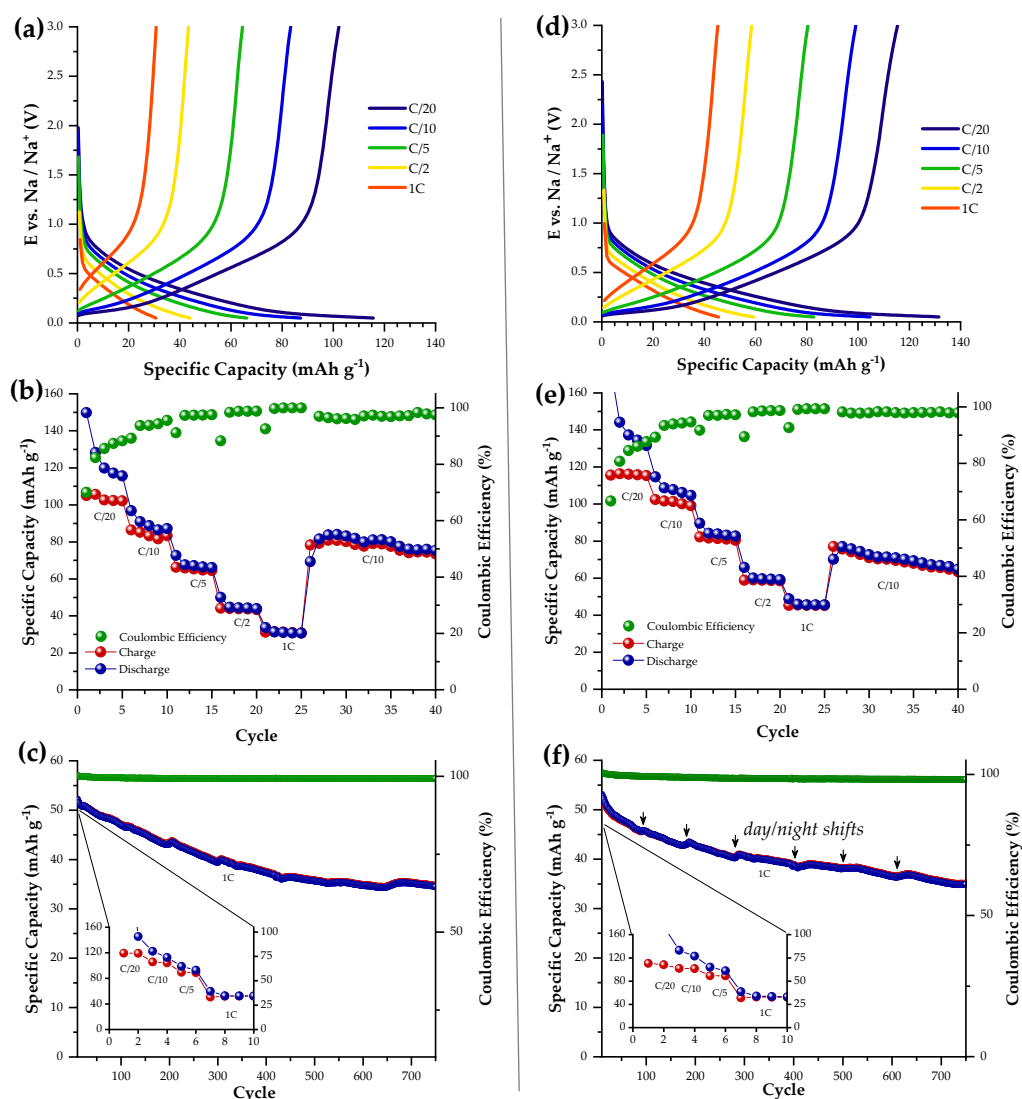
**Figure 7.** Galvanostatic cycling behavior of C-surgical (**a**–**c**) and C-FFP2 (**d**–**f**) with 1 M NaClO$_4$ in PC as electrolyte, in the 0.05–3 V vs. Na potential range: (**a**,**d**) Voltage vs. specific capacity profiles for selected cycles, one per current regime: C/20 (0.025 mA/cm$^2$), C/10 (0.05 mA/cm$^2$), C/5 (0.1 mA/cm$^2$), C/2 (0.25 mA/cm$^2$) and 1C (0.5 mA/cm$^2$); (**b**,**e**) Specific capacity and coulombic efficiency as a function of cycles at the five different current regimes; (**c**,**f**) Specific capacity and coulombic efficiency upon prolonged cycling at 1C; steps in the profiles were due to temperature oscillations upon day/night shifts.

Figure 7b,e shows the results of specific capacity plotted against the cycle number, underlining the capacity drop at a higher current. A lower initial coulombic efficiency was correlated to initial irreversible processes, i.e., the above-discussed SEI formation taking place in the initial cycles. However, in the initial cycles at the C/20 rate, the efficiency remained at relatively low values, indicating non-ideal stability of the formed SEI, which was more evident at low values at low current rates where parasitic reaction kinetics were favored. Nevertheless, the coulombic efficiency of both systems stabilized after the first 10 cycles, recovering up to 98% in the following cycling process. It is worth noting here that the coulombic efficiency might have been improved by the use of specific additives in the electrolyte, e.g., to stabilize the interface and allow enhanced SEI layer formation, thus reducing the initial irreversible capacity; however, this was out of the scope of the present work, which is simply demonstrating the easy and reliable repurposing of disposed FMs as NIB anodes after simple pyrolysis and no further activation protocols.

The other two Na-metal cells, utilizing either C-surgical or C-FFP2, were assembled for prolonged galvanostatic cycling up to 750 cycles (Figure 7c,f). The cycling protocol consisted of two cycles at C/20, C/10 and C/5 rates, followed by long-lasting cycling at 1C (i.e., at 0.5 mA/cm$^2$ based on the electrode constitution and on the envisaged theoretical specific capacity of 350 mAh g$^{-1}$). The capacity dropped by approximately 30% for both systems, although the coulombic efficiency remained above 98% throughout the whole measurement. The capacity oscillation visible during the cycling test was associated with day/night temperature variation, as the cells were tested under ambient laboratory temperatures and were not thermostatically stabilized upon cycling.

The C-surgical composite electrode showed a slightly higher coulombic efficiency compared to that of C-FFP2, exceeding 99.2% on average throughout the whole long-term constant-current cycling test. Thus, it was selected as the anode material for assembling the Na-ion cell using NVPF as the cathode. An NVPF cathode was recently demonstrated as an effective positive electrode material for Na batteries, operating at a moderately high voltage with three main redox reactions at ca. 3.4, 3.6 and 4.2 V [32]. NaClO$_4$ in PC (1 M) was used as a standard electrolyte.

Figure 8a shows the overlapped voltage signature of the NVPF electrode (green curve) and the C-surgical electrode (purple curve), which were utilized to evaluate the proper cell balancing to assemble the full cell. The practical capacity delivered by the NVPF electrode was about 128 mAh g$^{-1}$, while the capacity delivered by the C-surgical electrode was about 120 mAh g$^{-1}$ at the selected current regime of 0.1 mA/cm$^2$, which approximately corresponded to a C-rate of C/5 for both electrodes. The full cell was assembled utilizing a C-surgical electrode with a capacity of 0.54 mAh and an NVPF electrode with a capacity of 0.62 mAh, hence having an N/P ratio of 0.87.
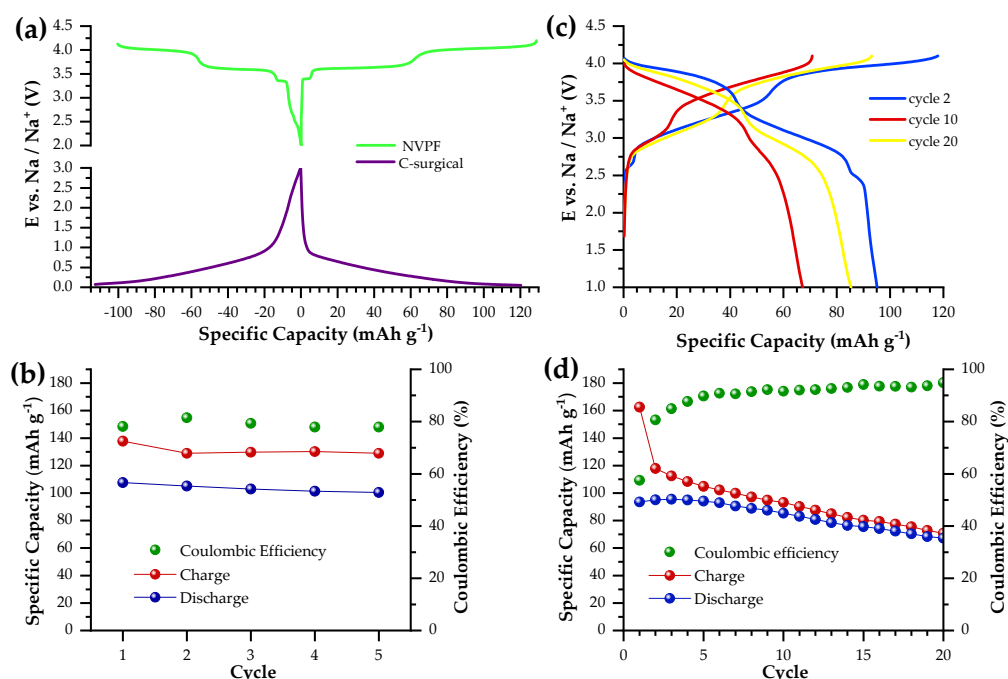


**Figure 8.** (**a**) Voltage (E) vs. specific capacity profiles at 0.1 mA/cm$^2$ for C-surgical anode and for NVPF cathode, both with 1 M NaClO$_4$ in PC as electrolyte vs. Na$^+$/Na. (**b**) Galvanostatic cycling behavior of NVPF at 0.1 mA/cm$^2$ vs. Na upon 5 cycles. (**c**) Voltage vs. specific capacity profiles at 0.1 mA/cm$^2$ for the full NVPF/(1 M) NaClO$_4$ in PC/C-surgical cell at selected cycles in the 1–4.1 V potential range vs. Na. (**d**) Specific capacity and coulombic efficiency of the full cell as a function of cycles upon prolonged cycling at 0.1 mA/cm$^2$ (C/5).

Before assembling the full cell, both electrodes were cycled separately in Na-metal cells for five cycles to compensate for the initial Na-consuming irreversible processes. The corresponding voltage profiles are shown in Figure 8a.

The measured specific capacity of NVPF (in Figure 8b) corresponded to the expected one in the charging process, while it was a little bit lower upon discharge, which limited the coulombic efficiency to 80%.

The voltage profiles (Figure 8c) of the full cell showed initial satisfying values of specific capacity, delivering almost 120 mAhg$^{-1}$ during charging. Upon cycling, a delivered capacity drop was evident, which was most likely associated with the relatively poor coulombic efficiency, thus leading to the Na-inventory depletion. The cell capacity decreased by about 47 mAhg$^{-1}$ at cycle 50, which was associated with an increase in the coulombic efficiency, which reached 95%, as seen in Figure 8d.

The assembling of a full-cell prototype represents a significant proof of concept for the eligibility of Na-ion batteries as a sustainable alternative to Li-ion ones, exploiting cheap and waste-recovered materials, especially in view of a possible scale-up of the production process.

## 4. Conclusions

The disposal of face masks represents a relevant environmental issue after the outbreak of the coronavirus pandemic in late 2019. In this work, we studied the pyrolytic conversion of surgical and FFP2 FMs into hard carbons (biochar) to be used as anode materials in post-lithium batteries, specifically Na-ion batteries. The recovery of a waste stream being our main purpose rather than the development of new materials for energy applications, we adopted mild conditions for the carbonization process; no chemical pretreatment of the FMs was used and pyrolysis was carried out at 800 °C in a $N_2$ atmosphere at ambient pressure for a relatively short time of 30 min. Both C-surgical and C-FFP2 combustion resulted in highly disordered carbons, the former characterized by bigger particles (up to 100 μm with respect to the submicrometric particles of C-FFP2).

Additionally, both C-surgical and C-FFP2 were effectively tested in laboratory-scale Na-metal cells (with $NaClO_4$ in PC as the electrolyte), displaying an acceptable specific capacity along with a wide range of current regimes from C/20 to 1C (i.e., from 0.025 mA/cm$^2$ to 0.5 mA/cm$^2$). Here as well, considering the purpose of the work, no post-synthesis material activation was carried out and no specific selection of electrolyte and/or other additives to stabilize the cell behavior was decided. Of course, further optimization of the preparation strategy and the final cell configuration are expected to lead to enhanced performance. Furthermore, as a proof of concept of real battery operation, C-surgical was employed within a full Na-ion cell in combination with an NVPF cathode, always using $NaClO_4$ in PC as electrolyte.

The results evidenced the possibility of obtaining amorphous carbon from face mask disposal in relatively mild conditions (no pretreatment, low pyrolysis temperature and short time). The electrochemical performance obtained in such conditions, still to be optimized in terms of specific capacity output to comply with the current commercial application standards, represents a preliminary confirmation of the effective repurposing of disposed face masks into higher-value materials for large-scale energy storage from renewables by Na-ion batteries. Overall, the information provided here can inspire future activities aiming to find a sustainable utilization of disposed materials, opening up new directions to innovate both the electrodes and even the full-cell technology by repurposing and revalorizing waste materials.

**Author Contributions:** Conceptualization, C.G.; FM pyrolysis and material characterization, M.B.; electrochemical tests and data analysis, S.P., A.P., N.P. and G.A.E.; NVPF preparation and testing, N.P., R.R.; writing, S.P., A.P. and M.B.; supervision, G.A.E., R.R., A.T. and C.G.; funding acquisition, C.G., A.T. and R.R. All authors have read and agreed to the published version of the manuscript.

**Conflicts of Interest:** The authors declare no conflict of interest.

## References

1. Dhama, K.; Khan, S.; Tiwari, R.; Sircar, S.; Bhat, S.; Malik, Y.S.; Singh, K.P.; Chaicumpa, W.; Bonilla-Aldana, D.K.; Rodriguez-Morales, A.J. Coronavirus disease 2019–COVID-19. *Clin. Microbiol. Rev.* **2020**, *33*, e00028-20. [CrossRef] [PubMed]
2. Fadare, O.O.; Okoffo, E.D. Covid-19 face masks: A potential source of microplastic fibers in the environment. *Sci. Total Environ.* **2020**, *737*, 140279. [CrossRef] [PubMed]
3. Dharmaraj, S.; Ashokkumar, V.; Hariharan, S.; Manibharathi, A.; Show, P.L.; Chong, C.T.; Ngamcharussrivichai, C. The COVID-19 pandemic face mask waste: A blooming threat to the marine environment. *Chemosphere* **2021**, *272*, 129601. [CrossRef] [PubMed]
4. Teymourian, T.; Teymoorian, T.; Kowsari, E.; Ramakrishna, S. Challenges, Strategies, and Recommendations for the Huge Surge in Plastic and Medical Waste during the Global COVID-19 Pandemic with Circular Economy Approach. *Mater. Circ. Econ.* **2021**, *3*, 6. [CrossRef]
5. Battegazzore, D.; Cravero, F.; Frache, A. Is it Possible to Mechanical Recycle the Materials of the Disposable Filtering Masks? *Polymers* **2020**, *12*, 2726. [CrossRef] [PubMed]
6. Sangkham, S. Face mask and medical waste disposal during the novel COVID-19 pandemic in Asia. *Case Stud. Chem. Environ. Eng.* **2020**, *2*, 100052. [CrossRef]
7. Torres, F.G.; De-la-Torre, G.E. Face mask waste generation and management during the COVID-19 pandemic: An overview and the Peruvian case. *Sci. Total Environ.* **2021**, *786*, 147628. [CrossRef]
8. Shanmugam, V.; Babu, K.; Garrison, T.F.; Capezza, A.J.; Olsson, R.T.; Ramakrishna, S.; Hedenqvist, M.S.; Singha, S.; Bartoli, M.; Giorcelli, M.; et al. Potential natural polymer-based nanofibres for the development of facemasks in countering viral outbreaks. *J. Appl. Polym. Sci.* **2021**, *138*, 50658. [CrossRef]
9. Voudrias, E.A. Technology selection for infectious medical waste treatment using the analytic hierarchy process. *J. Air Waste Manag. Assoc.* **2016**, *66*, 663–672. [CrossRef]
10. Sadhukhan, J.; Ng, K.S.; Hernandez, E.M. *Biorefineries and Chemical Processes: Design, Integration and Sustainability Analysis*; John Wiley & Sons, Ltd.: Hoboken, NJ, USA, 2014.
11. Park, C.; Choi, H.; Andrew Lin, K.-Y.; Kwon, E.E.; Lee, J. COVID-19 mask waste to energy via thermochemical pathway: Effect of Co-Feeding food waste. *Energy* **2021**, *230*, 120876. [CrossRef] [PubMed]
12. Lee, S.B.; Lee, J.; Tsang, Y.F.; Kim, Y.-M.; Jae, J.; Jung, S.-C.; Park, Y.-K. Production of value-added aromatics from wasted COVID-19 mask via catalytic pyrolysis. *Environ. Pollut.* **2021**, *283*, 117060. [CrossRef] [PubMed]
13. Zhu, Z.; Gao, F.; Zhang, Z.; Zhuang, Q.; Yu, H.; Huang, Y.; Liu, Q.; Fu, M. Synthesis of the cathode and anode materials from discarded surgical masks for high-performance asymmetric supercapacitors. *J. Colloid Interface Sci.* **2021**, *603*, 157–164. [CrossRef]
14. Yuwen, C.; Liu, B.; Rong, Q.; Zhang, L.; Guo, S. Self-activated pyrolytic synthesis of S, N and O co-doped porous carbon derived from discarded COVID-19 masks for lithium sulfur batteries. *Renew. Energy* **2022**, *192*, 58–66. [CrossRef]
15. Graedel, T.E. On the Future Availability of the Energy Metals. *Annu. Rev. Mater. Res.* **2011**, *41*, 323–335. [CrossRef]
16. Hirsh, H.S.; Li, Y.; Tan, D.H.S.; Zhang, M.; Zhao, E.; Meng, Y.S. Sodium-Ion Batteries Paving the Way for Grid Energy Storage. *Adv. Energy Mater.* **2020**, *10*, 2001274. [CrossRef]
17. Yabuuchi, N.; Kubota, K.; Dahbi, M.; Komaba, S. Research Development on Sodium-Ion Batteries. *Chem. Rev.* **2014**, *114*, 11636–11682. [CrossRef] [PubMed]
18. Usiskin, R.; Lu, Y.; Popovic, J.; Law, M.; Balaya, P.; Hu, Y.-S.; Maier, J. Fundamentals, status and promise of sodium-based batteries. *Nat. Rev. Mater.* **2021**, *6*, 1020–1035. [CrossRef]
19. Duffner, F.; Kronemeyer, N.; Tübke, J.; Leker, J.; Winter, M.; Schmuch, R. Post-lithium-ion battery cell production and its compatibility with lithium-ion cell production infrastructure. *Nat. Energy* **2021**, *6*, 123–134. [CrossRef]
20. You, Y.; Manthiram, A. Progress in High-Voltage Cathode Materials for Rechargeable Sodium-Ion Batteries. *Adv. Energy Mater.* **2018**, *8*, 1701785. [CrossRef]
21. Scrosati, B.; Garche, J. Lithium batteries: Status, prospects and future. *J. Power Sources* **2010**, *195*, 2419–2430. [CrossRef]
22. Chayambuka, K.; Mulder, G.; Danilov, D.L.; Notten, P.H.L. Sodium-Ion Battery Materials and Electrochemical Properties Reviewed. *Adv. Energy Mater.* **2018**, *8*, 1800079. [CrossRef]
23. Yoon, G.; Kim, H.; Park, I.; Kang, K. Conditions for Reversible Na Intercalation in Graphite: Theoretical Studies on the Interplay Among Guest Ions, Solvent, and Graphite Host. *Adv. Energy Mater.* **2017**, *7*, 1601519. [CrossRef]
24. Doeff, M.M.; Ma, Y.; Visco, S.J.; De Jonghe, L.C. Electrochemical Insertion of Sodium into Carbon. *J. Electrochem. Soc.* **1993**, *140*, L169–L170. [CrossRef]

25. Hou, H.; Qiu, X.; Wei, W.; Zhang, Y.; Ji, X. Carbon Anode Materials for Advanced Sodium-Ion Batteries. *Adv. Energy Mater.* **2017**, *7*, 1602898. [CrossRef]

26. Zhao, L.-F.; Hu, Z.; Lai, W.-H.; Tao, Y.; Peng, J.; Miao, Z.-C.; Wang, Y.-X.; Chou, S.-L.; Liu, H.-K.; Dou, S.-X. Hard Carbon Anodes: Fundamental Understanding and Commercial Perspectives for Na-Ion Batteries beyond Li-Ion and K-Ion Counterparts. *Adv. Energy Mater.* **2021**, *11*, 2002704. [CrossRef]

27. Xie, L.; Tang, C.; Bi, Z.; Song, M.; Fan, Y.; Yan, C.; Li, X.; Su, F.; Zhang, Q.; Chen, C. Hard Carbon Anodes for Next-Generation Li-Ion Batteries: Review and Perspective. *Adv. Energy Mater.* **2021**, *11*, 2101650. [CrossRef]

28. Piotrowska, A.; Kierzek, K.; Rutkowski, P.; Machnikowski, J. Properties and lithium insertion behavior of hard carbons produced by pyrolysis of various polymers at 1000 °C. *J. Anal. Appl. Pyrolysis* **2013**, *102*, 1–6. [CrossRef]

29. Shao, W.; Shi, H.; Jian, X.; Wu, Z.-S.; Hu, F. Hard-Carbon Anodes for Sodium-Ion Batteries: Recent Status and Challenging Perspectives. *Adv. Energy Sustain. Res.* **2022**, *3*, 2200009. [CrossRef]

30. Takenaka, N.; Bouibes, A.; Yamada, Y.; Nagaoka, M.; Yamada, A. Frontiers in Theoretical Analysis of Solid Electrolyte Interphase Formation Mechanism. *Adv. Mater.* **2021**, *33*, 2100574. [CrossRef] [PubMed]

31. Lee, G.; Eui Lee, M.; Kim, S.-S.; Joh, H.-I.; Lee, S. Efficient upcycling of polypropylene-based waste disposable masks into hard carbons for anodes in sodium ion batteries. *J. Ind. Eng. Chem.* **2022**, *105*, 268–277. [CrossRef]

32. Pianta, N.; Locatelli, D.; Ruffo, R. Cycling properties of Na$_3$V$_2$(PO$_4$)$_2$F$_3$ as positive material for sodium-ion batteries. *Ionics* **2021**, *27*, 1853–1860. [CrossRef]

33. Tagliaferro, A.; Rovere, M.; Padovano, E.; Bartoli, M.; Giorcelli, M. Introducing the Novel Mixed Gaussian-Lorentzian Lineshape in the Analysis of the Raman Signal of Biochar. *Nanomaterials* **2020**, *10*, 1748. [CrossRef] [PubMed]

34. Tuinstra, F.; Koenig, J.L. Raman Spectrum of Graphite. *J. Chem. Phys.* **1970**, *53*, 1126–1130. [CrossRef]

35. Song, W.; Ji, X.; Wu, Z.; Yang, Y.; Zhou, Z.; Li, F.; Chen, Q.; Banks, C.E. Exploration of ion migration mechanism and diffusion capability for Na3V2(PO4)2F3 cathode utilized in rechargeable sodium-ion batteries. *J. Power Sources* **2014**, *256*, 258–263. [CrossRef]

36. McDonald, M.P.; Ward, I.M. The assignment of the infra-red absorption bands and the measurement of tacticity in polypropylene. *Polymer* **1961**, *2*, 341–355. [CrossRef]

37. Burfield, D.R.; Loi, P.S.T. The use of infrared spectroscopy for determination of polypropylene stereoregularity. *J. Appl. Polym. Sci.* **1988**, *36*, 279–293. [CrossRef]

38. Hujuri, U.; Ghoshal, A.K.; Gumma, S. Temperature-dependent pyrolytic product evolution profile for polypropylene. *J. Appl. Polym. Sci.* **2011**, *119*, 2318–2325. [CrossRef]

39. Chan, J.H.; Balke, S.T. The thermal degradation kinetics of polypropylene: Part III. Thermogravimetric analyses. *Polym. Degrad. Stab.* **1997**, *57*, 135–149. [CrossRef]

40. Tuñón-Molina, A.; Takayama, K.; Redwan, E.M.; Uversky, V.N.; Andrés, J.; Serrano-Aroca, Á. Protective Face Masks: Current Status and Future Trends. *ACS Appl. Mater. Interfaces* **2021**, *13*, 56725–56751. [CrossRef]

41. Aboulkas, A.; El harfi, K.; El Bouadili, A. Thermal degradation behaviors of polyethylene and polypropylene. Part I: Pyrolysis kinetics and mechanisms. *Energy Convers. Manag.* **2010**, *51*, 1363–1369. [CrossRef]

42. Shimodaira, N.; Masui, A. Raman spectroscopic investigations of activated carbon materials. *J. Appl. Phys.* **2002**, *92*, 902–909. [CrossRef]

43. Orlando, A.; Franceschini, F.; Muscas, C.; Pidkova, S.; Bartoli, M.; Rovere, M.; Tagliaferro, A. A Comprehensive Review on Raman Spectroscopy Applications. *Chemosensors* **2021**, *9*, 262. [CrossRef]

44. Bartoli, M.; Giorcelli, M.; Jagdale, P.; Rovere, M.; Tagliaferro, A.; Chae, M.; Bressler, D.C. Shape tunability of carbonized cellulose nanocrystals. *SN Appl. Sci.* **2019**, *1*, 1661. [CrossRef]

45. Bartoli, M.; Nasir, M.A.; Jagdale, P.; Passaglia, E.; Spiniello, R.; Rosso, C.; Giorcelli, M.; Rovere, M.; Tagliaferro, A. Influence of pyrolytic thermal history on olive pruning biochar and related epoxy composites mechanical properties. *J. Compos. Mater.* **2020**, *54*, 1863–1873. [CrossRef]

46. Giorcelli, M.; Bartoli, M. Development of Coffee Biochar Filler for the Production of Electrical Conductive Reinforced Plastic. *Polymers* **2019**, *11*, 1916. [CrossRef] [PubMed]

47. Yousef, S.; Eimontas, J.; Stasiulaitiene, I.; Zakarauskas, K.; Striūgas, N. Pyrolysis of all layers of surgical mask waste as a mixture and its life-cycle assessment. *Sustain. Prod. Consum.* **2022**, *32*, 519–531. [CrossRef]

48. Carboni, M.; Manzi, J.; Armstrong, A.R.; Billaud, J.; Brutti, S.; Younesi, R. Analysis of the Solid Electrolyte Interphase on Hard Carbon Electrodes in Sodium-Ion Batteries. *ChemElectroChem* **2019**, *6*, 1745–1753. [CrossRef]

49. Vadhva, P.; Hu, J.; Johnson, M.J.; Stocker, R.; Braglia, M.; Brett, D.J.L.; Rettie, A.J.E. Electrochemical Impedance Spectroscopy for All-Solid-State Batteries: Theory, Methods and Future Outlook. *ChemElectroChem* **2021**, *8*, 1930–1947. [CrossRef]

50. Choi, W.; Shin, H.-C.; Kim, J.M.; Choi, J.-Y.; Yoon, W.-S. Modeling and Applications of Electrochemical Impedance Spectroscopy (EIS) for Lithium-ion Batteries. *J. Electrochem. Sci. Technol.* **2020**, *11*, 1–13. [CrossRef]

51. Zhang, R.; Xia, B.; Li, B.; Cao, L.; Lai, Y.; Zheng, W.; Wang, H.; Wang, W.; Wang, M. A Study on the Open Circuit Voltage and State of Charge Characterization of High Capacity Lithium-Ion Battery Under Different Temperature. *Energies* **2018**, *11*, 2408. [CrossRef]